Research Square

Preprints are preliminary reports that have not undergone peer review.
They should not be considered conclusive, used to inform clinical practice,
or referenced by the media as validated information.

Multi-field coupling response and storage efficiency of CO_2 sequestration in deep chambers considering capillary trapping and surrounding rock damage

Tian Zhichao

bailey280@163.com

Inner Mongolia University of Science and Technology

Zhang Yibo

Inner Mongolia University of Science and Technology

Liu Yejiao

Inner Mongolia University of Science and Technology

Li Songzhe

Inner Mongolia University of Science and Technology

Ma Lianyu

Inner Mongolia University of Science and Technology

Xiao Zhiwei

Inner Mongolia University of Science and Technology

Research Article

Keywords: Underground chamber, CO_2 sequestration, Thermal–hydraulic–mechanical (THM) coupling, Surrounding rock damage, Storage efficiency

Posted Date: November 13th, 2026

DOI: https://doi.org/10.21203/rs.3.rs-11364413/v1

License: This work is licensed under a Creative Commons Attribution 4.0 International License.
Read Full License

Additional Declarations: No competing interests reported.

Multi-field coupling response and storage efficiency of CO_2 sequestration in deep chambers considering capillary trapping and surrounding rock damage

Tian Zhichao[1,2,3,4], Zhang Yibo[1], Liu Yejiao[1,2,3,4], Li Songzhe[1], Ma Lianyu[1], Xiao Zhiwei[5]

[1]School of Mining and Coal Engineering, Inner Mongolia University of Science and Technology, Baotou 014010, China

[2]Key Laboratory of Mining Engineering of Inner Mongolia Autonomous Region, Inner Mongolia University of Science and Technology, Baotou 014010, China

[3]Engineering Technology Research Center for Safe Coal Mining and Utilization of Inner Mongolia Autonomous Region, Inner Mongolia University of Science and Technology, Baotou 014010, China

[4]Inner Mongolia Collaborative Innovation Center for Green Coal Mining and Utilization, Inner Mongolia University of Science and Technology, Baotou 014010, China

[5]School of Civil Engineering, Inner Mongolia University of Science and Technology, Baotou 014010, China

*Corresponding. bailey280@163.com.

ABSTRACT

In the face of global climate change, geological sequestration of carbon dioxide (CO_2) using underground space is a key pathway to achieving carbon emission reduction. In such engineering practices, storage efficiency and long-term safety directly constrain the technical feasibility of the project and its full life-cycle evolution. To investigate the safety, feasibility, and storage efficiency of CO_2 sequestration in deep chambers, this study combines physical experiments with numerical simulations to construct a thermal–hydraulic–mechanical (THM) three-field coupling model for CO_2 sequestration in abandoned mines, incorporating the dual effects of capillary pressure and surrounding rock damage. The storage safety and efficiency of CO_2 sequestration in deep chambers are then investigated. The results indicate that: (1) Under multi-field coupling, surrounding rock damage preferentially develops and propagates along the direction of higher initial in-situ stress, causing high-pressure CO_2 to preferentially form a dominant seepage pathway along this direction. (2) The seepage process of CO_2 is accompanied by significant heat exchange, leading to a marked temperature decrease in the surrounding rock of the chamber. This physical characteristic can serve as an important early warning indicator for monitoring concealed CO_2 leakage in practical engineering. (3) Storage depth has a significant nonlinear influence on CO_2 storage efficiency. As storage depth increases, the CO_2 storage efficiency of the chamber first increases and then decreases. When the depth increases from 500 m to 800 m, the storage efficiency increases by 0.76%; however, when the depth further increases from 800 m to 1200 m, the storage efficiency decreases by 0.24% due to factors such as high in-situ stress compaction. This study reveals the THM coupling mechanism of CO_2 sequestration in deep chambers under high-stress environments. It not only provides solid theoretical support for the large-scale resource utilization of underground space in abandoned mines, but also offers important scientific basis and engineering guidance for the scheme design and long-term safety evaluation of future deep geological carbon sequestration projects.

Keywords: Underground chamber; CO_2 sequestration; Thermal–hydraulic–mechanical (THM) coupling; Surrounding rock damage; Storage efficiency

Article Highlights

1.Surrounding rock damage controls the direction of preferential CO_2 seepage pathways.

2.Temperature decrease during CO_2 seepage can serve as an early leakage warning indicator.

3.A nonlinear depth–efficiency relationship reveals an optimal depth window for storage.

1.Introduction

The continuous increase in atmospheric carbon dioxide (CO_2) concentration, which drives the greenhouse effect and climate change, poses a severe global challenge. To achieve the strategic goals of "carbon peaking" and "carbon neutrality," developing efficient and safe carbon capture, utilization, and storage (CCUS) technologies has become an inevitable choice. Among the various CO_2 storage pathways, geological storage has become mainstream due to its enormous potential and relatively mature technology. However, conventional geological storage (e.g., deep saline aquifers and depleted oil and gas reservoirs) imposes stringent site requirements: reservoirs must possess high permeability, caprocks must be dense and intact, and deep temperature–pressure variations pose significant challenges to long-term safety. In contrast, CO_2 storage in deep underground chambers offers unique advantages. Abandoned underground large-scale structures exhibit stable surrounding rock and favorable sealing capacity, allowing temporary CO_2 storage and on-demand extraction, which facilitates carbon resource recycling. Meanwhile, the injected high-pressure gas can partially offset the in-situ stress of the deep surrounding rock, substantially reducing long-term maintenance costs. Therefore, investigating CO_2 storage in underground chambers carries dual strategic significance for environmental protection and the reuse of underground space resources.

In underground chamber CO_2 storage engineering, storage efficiency and long-term safety are the core evaluation criteria. To ensure the stable retention of high-pressure gas under complex geological conditions, long-term monitoring of the CO_2 plume migration front and distribution characteristics is often required. Given the high cost and risk of large-scale in-situ experiments, multi-physics numerical simulation has become an important means to investigate CO_2 migration behavior and assess leakage risk. To date, scholars have conducted in-depth studies on the influence of surrounding rock mechanical parameter evolution and fluid phase transition on storage performance. On the one hand, the dynamic response of reservoir physical properties significantly constrains storage capacity: (Yin et al. 2023) found that water saturation and porosity directly affect storage capacity; (Guo et al. 2019) explored diffusion and adsorption mechanisms under low-permeability conditions; (Peng et al. 2025), relying on the Sleipner project, revealed that increasing saturation in a CO_2–brine two-phase system leads to a decrease in bulk modulus and wave velocity. On the other hand, CO_2 phase evolution under deep extreme temperature–pressure conditions has also attracted attention: (Dan et al. 2025) found a nonlinear surge in capillary breakthrough pressure near the gas–liquid phase transition point; (Lei et al. 2025) experimentally confirmed that supercritical CO_2 can significantly dissolve and alter reservoir structure, sharply increasing rock porosity and permeability. These fundamental studies vividly characterize fluid migration behavior and lay a solid foundation for understanding deep CO_2 storage mechanisms.

Despite the beneficial exploration of CO_2 storage in underground space, fine-scale multi-field coupling studies focusing on a single large-scale underground chamber remain notably limited. First, existing physical experiments are mostly confined to small-scale reduced-scale tests under a single physical field, making it difficult to realistically and long-term reflect the dynamic migration behavior of CO_2 in formations under complex high-stress environments. Second, existing multi-physics coupling simulations often adopt simple, idealized constitutive models, and the characterization of CO_2 migration largely relies on fixed permeability and porosity, failing to fully consider the key factor hindering CO_2 migration in deep ultra-low-permeability surrounding rock pores—the capillary trapping effect (Cui et al. 2023; Yao et al. 2023; Guo et al. 2019). Moreover, the true dynamic coupling mechanism between capillary pressure and rock mechanical damage is rarely incorporated into calculations. To more systematically and realistically evaluate the safety and efficiency of CO_2 storage in deep underground chambers, this study combines physical experiment-based parameter assignment with large-scale numerical simulation to construct a thermal–hydraulic–mechanical (THM)

three-field coupling numerical model that comprehensively considers capillary trapping effects and surrounding rock mechanical damage evolution. The stress response of the chamber surrounding rock, CO_2 seepage and temperature field evolution, and final storage efficiency under different storage depths and initial injection pressures are systematically analyzed. The research results can provide a reliable theoretical basis and numerical reference for target area selection, scheme design, and risk assessment of future underground CO_2 storage projects.

2. Physical Experiment on CO_2 Sequestration

2.1 Experimental Preparation

The granite blocks used in this experiment were collected from the Xiaoyun Coal Mine in Jining, Shandong Province. Following the standard for engineering rock mass test methods, cylindrical specimens of Φ50 mm × 100 mm were obtained by core drilling, as shown in Figure 1. Ultrasonic testing was performed on the specimens using an ultrasonic apparatus, and samples with approximately identical wave velocities (variation < 5%) were selected for the experiments.



Figure 1. Granite specimens

The experiment employed a deep formation CO_2 injection control and monitoring simulation system (Figure 2). This system comprises a triaxial pressure chamber, a confining pressure and high-temperature loading control system, a seepage loading system, a CO_2 cylinder, an axial loading system, and a data acquisition system, enabling multi-field coupling experiments under CO_2 seepage conditions.

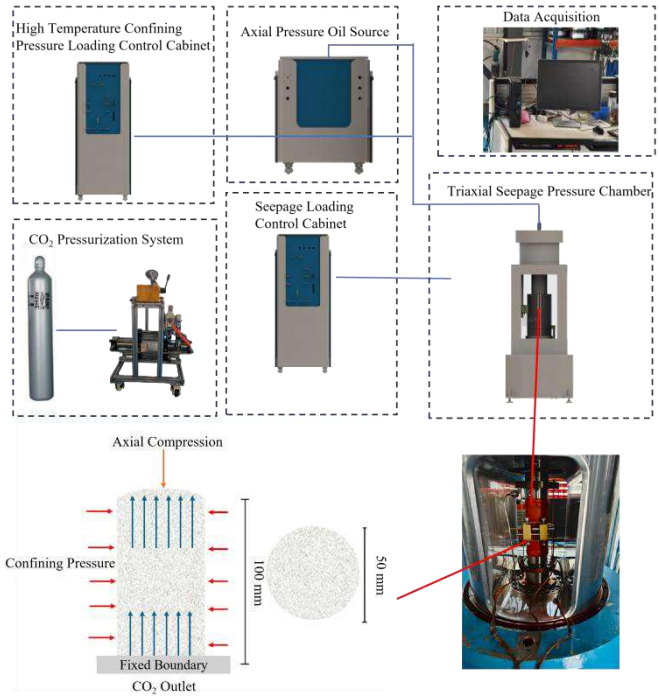


Figure 2. Experimental apparatus

The loading path of this triaxial seepage test is shown in Figure 3, adopting a combined stress and displacement control mode. The specific loading steps are as follows:

(1) Specimen installation and sealing: The granite specimen, sealed with a heat-shrinkable sleeve, was placed in the triaxial pressure chamber. The upstream and downstream seepage pipelines were connected, and the system airtightness was strictly checked.

(2) Constant confining pressure loading: Axial pressure and confining pressure were simultaneously applied to the target values (12, 18, or 27 MPa), after which the confining pressure was kept constant to simulate the initial horizontal in-situ stress of the deep chamber.

(3) Constant seepage pressure loading: CO_2 was slowly injected into the specimen to a preset pressure (5, 8, or 10 MPa) and fully stabilized to achieve dynamic equilibrium of the pore fluid. During this process, the confining pressure was always strictly greater than the CO_2 pressure to prevent gas leakage.

(4) Axial failure loading: Under constant confining pressure and CO_2 pressure, the displacement control mode was adopted to increase the axial pressure linearly with time until macroscopic fracture failure of the specimen occurred, while multi-field coupling data throughout the loading process were recorded in real time.

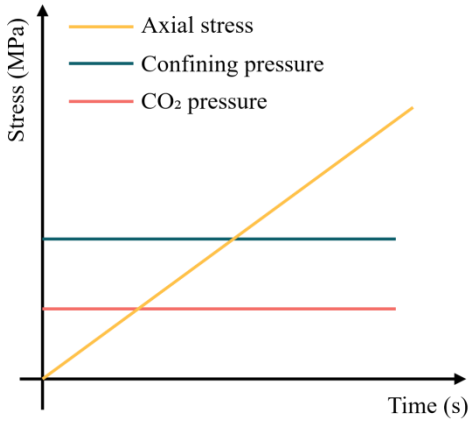


Figure 3. Loading path

2.2 Experimental Results Analysis and Parameter Acquisition

Given that the stress–strain curves of granite under different conditions are basically consistent in shape, this study takes the granite specimen as an example and summarizes its fracture deformation process into five consecutive typical stages. The first stage is the pore compaction stage (OA segment). As the load is applied, the primary micro-pores and fissures within the rock are gradually compacted and closed, resulting in a concave-down characteristic of the initial curve. Subsequently, the specimen transitions to the elastic deformation stage (AB segment), where stress and strain exhibit a fully linear relationship, and the rock undergoes recoverable elastic volumetric contraction under axial pressure. Once the load exceeds the elastic limit (point B), the curve begins to deviate from a straight line with a decreasing slope, marking the entry of the specimen into the plastic yield stage (BC segment). During this period, irreversible plastic damage and micro-cracks initiate and accumulate within the rock until the peak strength is reached at point C. Upon crossing the peak, the specimen enters the post-peak failure stage (CD segment), characterized by a significant drop in macroscopic stress and a sharp increase in strain. Internal micro-cracks rapidly propagate, coalesce, and form macroscopic fracture surfaces, causing a substantial decline in the bearing capacity of the rock mass. Finally, after the macroscopic fracture surface is fully formed, the specimen enters the residual strength stage (DE segment), where the fractured rock blocks mainly rely on friction between fracture surfaces to maintain load bearing. The stress state tends to stabilize with only minor fluctuations, exhibiting overall stable residual strength characteristics.

To investigate the influence of confining pressure and CO_2 pressure on the mechanical properties of granite specimens, triaxial seepage tests were conducted under different confining pressures and different CO_2 pressures. The stress–strain curves of granite under different confining pressures and CO_2 pressures are shown in Figure 4.

To explore the mechanical response characteristics of granite under different conditions, this study systematically extracted the peak stress and peak strain parameters from the experimental data (see Table 1 and Figure 4 for details). Comprehensive analysis reveals that confining pressure and CO_2 pressure exhibit opposite regulatory mechanisms on the mechanical properties of granite. On the one hand, confining pressure has a significant strengthening effect on rock strength. As a typical porous medium material, the natural micro-cracks and pores within granite are gradually compacted and closed under increasing confining pressure. This not only allows the rock to undergo more sufficient plastic deformation before failure, but also, due to the improvement of meso-structural integrity, causes the peak stress and strain of the specimen to show a clear increasing trend with rising confining pressure (for example, under a CO_2 pressure of 5 MPa, confining pressures of 12 MPa, 18 MPa, and 27 MPa increased the peak strength by 21%, 68%, and 78.4%, respectively, compared with uniaxial compression). In contrast, CO_2 fluid pressure exhibits a weakening effect on rock-bearing capacity. Under the same confining pressure, the peak stress of the specimen shows a clear negative correlation with CO_2 pressure. According to the effective stress principle, the increase in pore fluid pressure caused by CO_2 injection directly reduces the effective stress acting on the granite skeleton. This not only prolongs the closure stage of internal defects but also macroscopically leads to a decline in skeleton bearing capacity (for example, under a confining pressure of 12 MPa, when CO_2 pressure increased from 5 MPa to 8 MPa and 10 MPa, the peak stress decreased by 2.8% and 4.1%, respectively).

Table 1. Peak stress change rate and peak strain of granite specimens

CO_2 pressure	Confining pressure 12 MPa		Confining pressure 18 MPa		Confining pressure 27 MPa	
/MPa	$\Delta\sigma_{max}$	ε_{max}(%)	$\Delta\sigma_{max}$	ε_{max}(%)	$\Delta\sigma_{max}$	ε_{max}(%)
5	21%	1.17	68%	1.37	78.4%	1.40
8	17.7%	1.20	65%	1.38	77.3%	1.43
10	12.8%	1.25	58%	1.41	73%	1.42

Based on the above mechanical evolution laws, this triaxial seepage test not only reveals the fracture response characteristics of chamber surrounding rock under deep environments, but also determines the basic mechanical and seepage parameters of this typical high-strength surrounding rock. The experimental results show that the elastic modulus of the granite ranges from 38.1 to 40 GPa, and the initial permeability magnitude exhibits the characteristics of an extremely low-permeability medium. These material parametersrs obtained from real physical experiments effectively avoid the defect of idealized parameter values in conventional simulations, providing reliable underlying data support for the subsequent construction of a large-scale thermal–hydraulic–mechanical (THM) multi-field coupling numerical model for deep underground chambers (specific input parameters for numerical simulation are detailed in Table 2 later).

Table 2. Material parameters of surround

Density ρ (kg/m³)	Elastic modulus E (GPa)	Permeability k (m²)	Porosity (φ)	Poisson's ratio (ν)	Internal friction angle (°)
2500 kg/m3	40 GPa	1×10-18m2	0.15	0.25	35°

3. Multi-field Coupling Model Construction and Simulation Design

3.1 Governing Equations of Multi-physical Fields

The governing equation of solid mechanics is:

$$Gu_{i,ji} + \frac{G}{1-2\mu}u_{j,ji} + \alpha p_{,i} + F_i + K\alpha_T T_i = 0 \tag{1}$$

where the third term represents the influence of fluid on stress, Fi denotes the body force, and the fifth term represents the influence of temperature on stress.

The governing equation of the temperature field mainly involves the flow and heat transfer of CO_2, as well as the influence of temperature variation on the damage variable. The thermal stress is calculated as:

$$\sigma_T = E\Delta T\alpha_T \tag{2}$$

Where σ_T is the thermal stress (MPa), E is the elastic modulus of the rock (GPa), α_T is the thermal expansion coefficient (1/K), and ΔT is the temperature difference between the rock and the fluid (K).

The CO_2 flow and heat transfer process requires coupling with the Darcy field velocity. The governing equation is:

$$(\rho C_p)_{\text{eq}}\frac{\partial T}{\partial t} + \rho_j C_{p_j}\mathbf{v}_f \cdot \nabla T = \nabla \cdot (\lambda_{\text{eq}}\nabla T) + Q_b \tag{3}$$

Where Q_b is the heat source term, which is reflected in the simulation as the geothermal gradient (W/m³). The first term is the equivalent volumetric heat capacity of the porous medium, expressed as:

$$(\rho C_p)_{eq} = (1-\phi)\rho_s C_{p_s} + \phi(S_g\rho_g C_{p_g} + S_s\rho_s C_{p_s}) \tag{4}$$

Where ϕ is the porosity, ρ_s and ρ_g are the densities of the rock skeleton and CO_2, respectively , C_{ps} and C_{pg} are the specific heat capacities of the rock skeleton and CO_2, respectively, and S_g is the saturation of supercritical CO_2. The second term is the fluid convection term, expressed as:

$$\rho_g C_{p_g} v_g = \rho_g C_{p_g} v_g \tag{5}$$

Where v_g is the CO_2 seepage velocity. λ_{eq} is the equivalent thermal conductivity, calculated as:

$$\lambda eq = (1-\phi)\lambda s + \phi(Sg\lambda g + Ss\lambda s) \tag{6}$$

Where λ_s and λ_g are the thermal conductivities of the rock skeleton and CO_2, respectively.

The damage constitutive model of the rock adopts the Mohr–Coulomb criterion and the maximum tensile stress criterion, as shown in Eqs.(7)-(9):

$$F_1 = -\sigma_1 - f_t \tag{7}$$

$$F_2 = \sigma_1 - \sigma_3 \frac{1+\sin\varphi}{1-\sin\varphi} - f_c \tag{8}$$

$$D = \begin{cases} 0 & (F_1 < 0, F_2 < 0) \\ 1 - \left|\dfrac{\varepsilon_t}{\varepsilon_3}\right|^n & (F_1 = 0, dF_1 > 0) \\ 1 - \left|\dfrac{\varepsilon_c}{\varepsilon_1}\right|^m & (F_2 = 0, dF_2 > 0) \end{cases} \tag{9}$$

Where f_t is the tensile strength and f_c is the compressive strength. The damage criterion of the model is based on the Mohr–Coulomb and maximum tensile stress criteria, but the influence of thermal stress on damage needs to be coupled in both criteria. The expression is:

$$F = \sigma 1 - \frac{1-sin\phi}{1+sin\phi}\sigma 3 - \sigma c(T) \le 0 \tag{10}$$

where the compressive strength is a function of temperature. The compressive strength after coupling with temperature is:

$$\sigma_c(T) = \sigma_{c0} exp[-k(T - T_0)] \tag{11}$$

Where σ_{c0} is the compressive strength at the initial temperature, and k is the temperature influence coefficient, taken as $2.7\times10-3(1/^\circ$ C) according to the literature.

Rock damage affects the elastic modulus, permeability, and porosity of the rock, as shown in Eqs. (12)–(14):

$$E = (1-D)E_0 \tag{12}$$

$$\phi = \phi_0 + D(\phi_r - \phi_0) \tag{13}$$

$$K = K_0 \left(\frac{\phi}{\phi_0}\right)^3 e^{\alpha_k D} \tag{14}$$

Where E_0 is the initial elastic modulus, ϕ_0 is the initial porosity, ϕ_r is the residual porosity, and α_k is the influence coefficient of damage on the matrix permeability of the rock mass, taken as 5×10^{-8} Pa^{-1} in this study.

To better fit engineering practice and prevent physical distortion, the gas in the chamber cannot fully flow out through seepage. Therefore, a permeability correction model coupled with saturation damage is introduced in this model. According to Eq. (14), damage increases the permeability of the surrounding rock, as shown in Eq. (15). To simulate the self-sealing system of the chamber, saturation is introduced to perform a secondary

correction on the permeability, as follows:

$$k_{eff} = k(D) * k_s \tag{15}$$

Where k_{eff} is the effective permeability, $k(D)$ is the permeability corrected by the damage variable, and k_s is the saturation correction coefficient.

The saturation correction coefficient is set to two states according to the Brooks–Corey capillary pressure model, and the switching function is:

$$ks = \begin{cases} (\frac{S_g - S_{gr}}{1 - S_{gr}})^n & S_g > S_{gr} \\ 0 & S_g \leqslant S_{gr} \end{cases} \tag{16}$$

Where S_g is the saturation and S_{gr} is the residual saturation, taken as 0.3(Wang et al. 2025; Wang et al. 2023; Hu 2021) according to previous studies.

The mass conservation equation of fluid seepage is shown in Eq. (17), and the momentum equation is given by Darcy's law as shown in Eq. (18):

$$\rho S \frac{\partial \rho}{\partial t} + \nabla \cdot (\rho U) = Q_{\mathrm{m}} \tag{17}$$

$$U = -\frac{K}{v} \Delta p \tag{18}$$

Where ρ is the fluid density, S is the storage coefficient, and U is the Darcy velocity. To simulate the migration of CO_2, a porous medium species transport interface is used, and the main governing equation is Fick's second law:

$$\frac{\partial c}{\partial t} = D\nabla^2 c + R \tag{19}$$

Where C is the CO_2 concentration and D is the diffusion coefficient. The governing equation corrected based on the porous medium is:

$$\frac{\partial (\varepsilon \cdot c)}{\partial t} = \nabla \cdot (Deff \cdot \nabla c) + R \tag{20}$$

Where D_{eff} is the effective diffusion coefficient, and R is the source term, which is positive here, indicating that CO_2 flows into the surrounding rock.

3.2 Governing Equation for Storage Efficiency

CO_2 follows mass conservation during seepage along the chamber wall. The rate of mass decrease of gas inside the chamber equals the total mass flow rate flowing out of the chamber boundary, which gives:

$$M_v = \frac{d}{dt}(m_v) = -\int_\Gamma \rho \mathbf{u} \cdot \mathbf{n} d\Gamma \tag{21}$$

Where m_v is the gas mass inside the chamber? The left side represents the mass decrease of CO_2 inside the chamber, and the right side represents the total mass flow rate of CO_2 flowing out of the chamber boundary. m_v is obtained from the ideal gas equation, expressed as:

$$m_d = \frac{PVM_{co2}}{RT} \tag{22}$$

Where p is the chamber pressure, V is the chamber volume, M is the molar mass of CO_2, RR is the specific gas constant, and TT is the temperature at the current moment.

In this model, the chamber is a cylindrical chamber with a base radius of 5 m and a height of 5 m, with a volume of 392.5 m^3. The initial temperature is the geothermal temperature of 299.15 K. Taking a CO_2 pressure of 5 MPa as an example, the initial storage amount is 35.4 t CO_2.

3.3 Establishment of the Numerical Simulation Model

Although the physical experiments in Section 2 successfully obtained the basic mechanical and seepage parameters of the chamber surrounding rock, the size effect of laboratory specimens makes it difficult to fully reflect the dynamic evolution characteristics of the thermal–hydraulic–mechanical (THM) multi-physical fields in a deep, large-scale chamber during long-term storage. To overcome this spatial limitation, this study integrates the measured parameters with the aforementioned multi-field coupling governing equations and conducts a large-scale numerical simulation to systematically and quantitatively evaluate the storage safety and actual storage efficiency of the deep underground chamber.

Since the research focus is on the evolution laws of temperature, stress, and permeability in the chamber surrounding rock during long-term high-pressure CO_2 storage, as well as the CO_2 storage efficiency of the deep underground chamber, the CO_2 injection process is simplified in the model. It is assumed that the chamber is already filled with CO_2 at the initial moment of simulation. The two-dimensional large-scale numerical model for CO_2 storage in the deep underground chamber is shown in Figure 5. The chamber radius is set to 5 m. To avoid size effects, the formation is established as 80 × 80 m, with the chamber located at the center of the formation. The top surface of the formation corresponds to a depth of −460 m. According to the coordinate system in Figure 6, the center of the chamber is located at (40, 40), the top surface of the formation is at y = 40 m, and the left and right boundaries are at x = 0 m and x = 80 m, respectively.

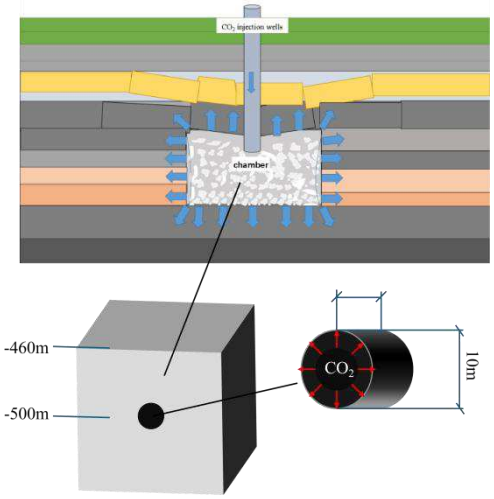


Figure 5. Schematic diagram of the simulation model

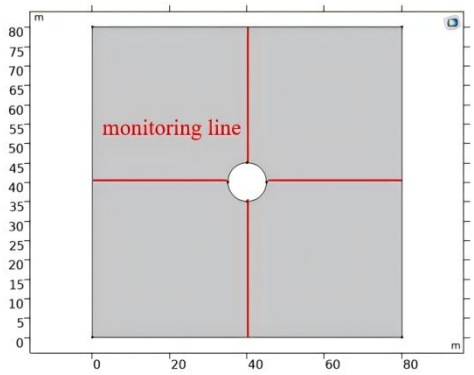


Figure 6. Chamber model

3.4 Boundary Conditions of the Numerical Simulation

Figure 7 presents the initial and boundary conditions of the numerical model. Taking the storage case at a depth of 500 m as an example, the top boundary of the model corresponds to an actual formation depth of −460 m. Regarding the mechanical boundary and initial stress field, the overlying rock mass is assumed to be a homogeneous and isotropic medium. Based on the self-weight stress formula, an initial vertical in-situ stress of 11.5 MPa is applied to the top surface of the model. The horizontal in-situ stress is influenced by the depth gradient, and a trapezoidal horizontal load distribution is applied to the lateral boundaries of the model. Regarding the seepage boundary and initial fluid field, the chamber wall is set as a constant-pressure injection boundary with a CO_2 fluid pressure of 5 MPa, while the initial pore fluid pressure within the surrounding rock is set to 0 MPa.

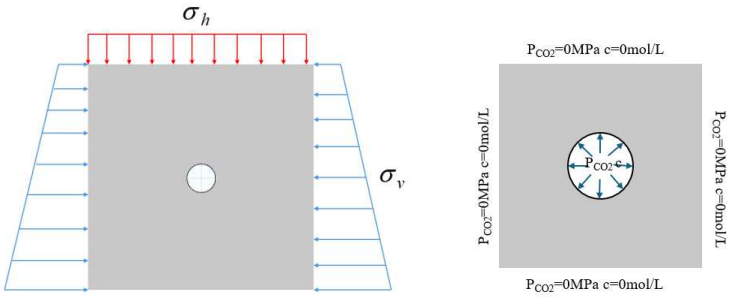
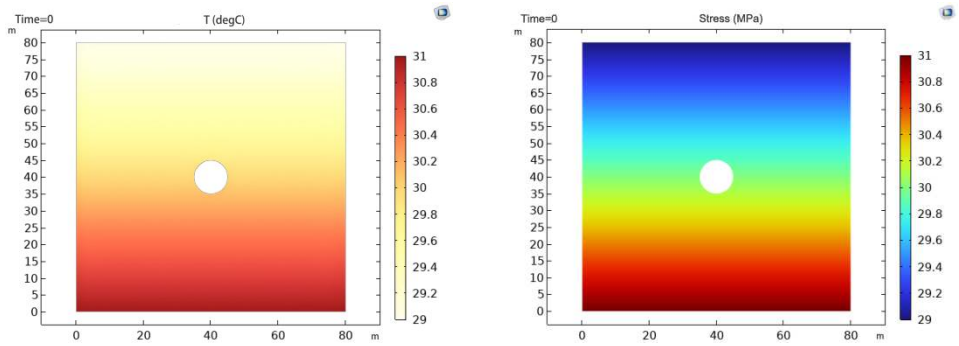


Figure 7. Boundary conditions

The initial temperature field distribution is similar to that of the in-situ stress field and is calculated according to a geothermal gradient of 25 ° C/km. Figure 8 shows the initial temperature distribution and in-situ stress distribution.



(a) Initial temperature field distribution (b) Initial vertical in-situ stress distribution

Figure 8. Initial values of the temperature field and stress field

3.5 Design of Numerical Simulation Cases

In CO_2 geological storage engineering, CO_2 is typically pressurized to an appropriate storage pressure according to the in-situ stress at the storage depth, so as to prevent chamber surrounding rock failure or low storage efficiency caused by excessively high or low gas pressure. Based on the in-situ stress calculation formula and the CO_2 phase distribution, three storage depths were selected, covering shallow, intermediate, and deep depths. The corresponding storage pressures and geothermal temperatures at these depths were calculated, and the simulation cases are listed in Table 3.

Table 3. Simulation cases for CO_2 storage

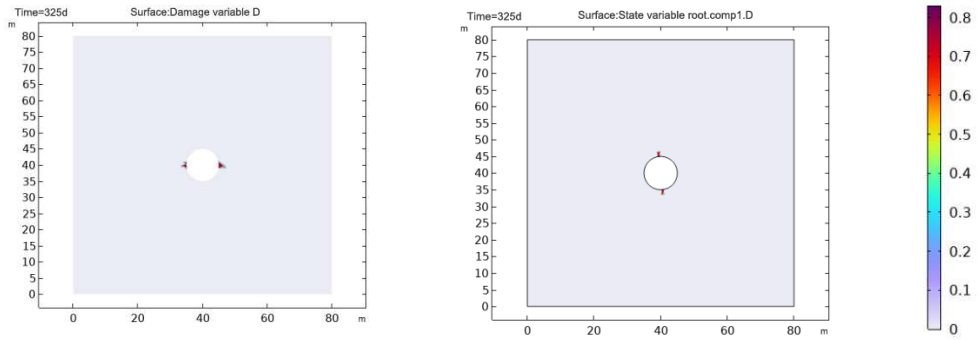
case	Depth (m)	Storage pressure (MPa)	Temperature (°C)	Phase state
1	500	5	27.5	Gaseous
2	800	7.5	35	Supercritical
3	1200	10	45	Supercritical

4. Results and Discussion

The numerical model in this study is a thermal–hydraulic–mechanical (THM) three-field coupling model. The simulation covers the period from the initial moment, when CO_2 has been fully injected into the chamber, to one year of storage. The behavior of different physical fields at different times is investigated separately. Since the cloud map evolution of the three cases is nearly identical across all physical fields, Case 1 is taken as an example to analyze the variation trends of each physical quantity during chamber storage.

4.1 Solid Mechanics Analysis

Based on the numerical simulation results, the damage cloud map and stress distribution of the chamber surrounding rock are presented in Figure 9. Figure 9 illustrates two scenarios with different magnitudes of horizontal and vertical in-situ stresses. In Figure 9(a), the horizontal in-situ stress is greater than the vertical in-situ stress; in Figure 9(b), the horizontal in-situ stress is smaller than the vertical in-situ stress. When the horizontal in-situ stress is greater than the vertical in-situ stress, damage occurs at the left and right sidewalls of the chamber; otherwise, it occurs at the roof and floor. In other words, damage always develops along the direction of greater in-situ stress.



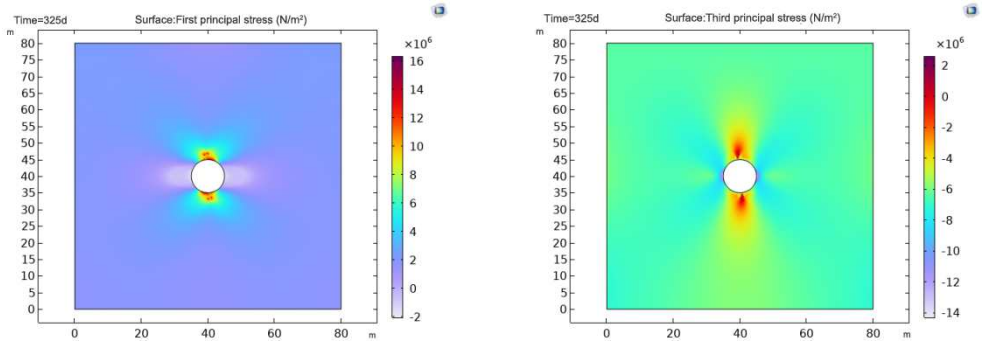
(a) Damage cloud map when the horizontal in-situ stress is greater

(b) Damage cloud map when the vertical in-situ stress is greater

Figure 9. Damage cloud maps

Taking the case of greater vertical in-situ stress as an example, according to the Mohr–Coulomb criterion and the maximum tensile stress criterion, shear and tensile failure are most likely to occur at the locations where the first and third principal stresses are most critical. Figure 10 shows the first and third principal stress distributions of the chamber surrounding rock for the case where the vertical in-situ stress is greater than the

horizontal in-situ stress. It can be seen that both the first and third principal stresses reach their maximum values at the roof and floor of the chamber, which is consistent with the damage variable distribution. This indicates that in CO_2 storage projects using abandoned mine underground chambers, monitoring should be carried out at the roof and floor or at the left and right sidewalls according to the measured in-situ stress distribution, so as to prevent CO_2 leakage caused by chamber failure.

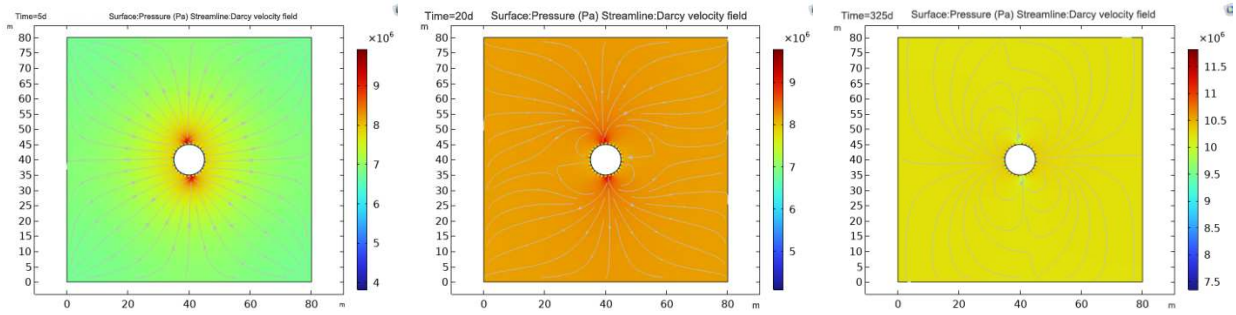


(a) First principal stress distribution (b) Third principal stress distribution

Figure 10. Stress cloud maps

4.2 Flow and Mass Transfer Field Analysis

In this simulation, the Darcy field is coupled with a dilute species transport interface to investigate CO_2 seepage in the chamber. Figure 11 presents the pressure cloud maps of the chamber at different time nodes. As shown in Figure 11, at the initial moment, the pressure around the surrounding rock is relatively low and mainly concentrated at the floor and roof of the chamber. At this stage, CO_2 primarily seeps through the surrounding rock at the roof and floor. According to the above analysis of the solid field, this is because damage occurs at the roof and floor of the chamber, which increases the permeability and porosity of the rock at the damaged locations and forms preferential pathways for CO_2 seepage. As time progresses, the surrounding rock pressure gradually approaches that at the roof and floor of the chamber. The main seepage pathways for CO_2 remain at the roof and floor; however, the seepage velocity decreases significantly due to the reduced pressure difference with the surrounding rock.



(a) Time = 5 d (b) Time = 20 d (c) Time = 325 d

Figure 11. Pressure cloud maps

To more intuitively observe the variation of CO_2 seepage pressure in the chamber surrounding rock, domain integration of the fluid pressure over the entire surrounding rock domain was performed, yielding the curve of total pressure in the surrounding rock over time, as shown in Figure 12. The gas pressure in the surrounding rock gradually increases over time, rising rapidly in the first 20 days and then slowing down after 20 days. The rapid pressure increase in the first 20 days is mainly attributed to two factors: first, the large pressure difference between the high-pressure gas inside the chamber and the low gas pressure in the surrounding rock drives rapid gas migration into the surrounding rock; second, CO_2 injection into the chamber causes a sudden increase in

chamber surrounding rock damage, allowing CO_2 to penetrate more rapidly at the damaged locations.

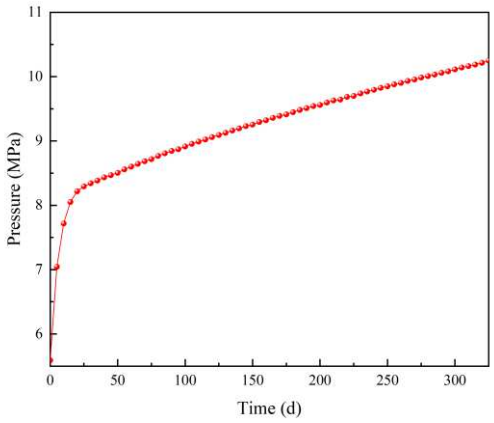
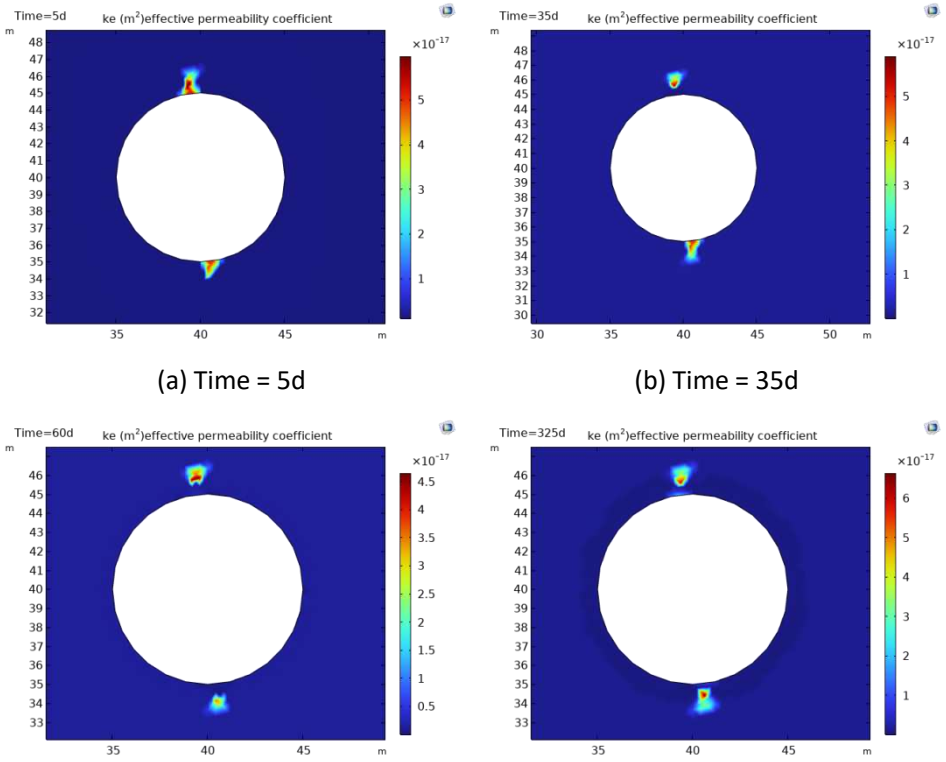


Figure 12. Pressure–time curve of the surrounding rock

According to the governing equations described in Section 3, to describe the retention phenomenon of CO_2 in the surrounding rock caused by capillary pressure, the K–C model is adopted. The CO_2 saturation and residual CO_2 saturation are introduced, and the seepage characteristics of the surrounding rock are secondarily corrected through the numerical relationship between Sg and Sgr in the surrounding rock. The corrected permeability distribution cloud map is shown in Figure 13.



(a) Time = 5d (b) Time = 35d

(c) Time = 60 d (d) Time = 325 d

Figure 13. Permeability evolution cloud maps

The permeability evolution exhibits distinct staged characteristics and can be divided into three stages. The first stage is the permeability change caused by damage (0–35 d). Except at the roof and floor of the chamber, the permeability of the surrounding rock remains at its initial value, and only the permeability at the roof and floor changes significantly. This is because, in the early stage, CO_2 has not fully entered the surrounding rock,

and the CO_2 saturation in the surrounding rock is far below the residual CO_2 saturation. At this stage, the permeability evolution is mainly governed by damage. According to the damage analysis of the chamber, damage occurs in the surrounding rock at the roof and floor, which explains the permeability changes at these locations.

The second stage is the permeability change caused by the coupling of damage and capillary pressure (35–60 d). At this stage, the permeability at the surfaces of the roof and floor gradually decreases and becomes consistent with that of the surrounding rock, but the permeability at a certain distance from the surface still changes considerably. To more intuitively illustrate the causes of permeability changes in the second stage, Figure 14 presents a schematic diagram of the permeability variation in the second stage. The regions with more pronounced permeability changes are divided into a top band and a bottom band. Taking the top band as an example, at the chamber surface, the presence of the damage variable increases the porosity of the surrounding rock, and CO_2 seeps more rapidly at the damaged locations. More CO_2 enters and is stored in the pores of the chamber surrounding rock, causing faster changes in CO_2 saturation. After correction by the capillary pressure model, the locations with faster seepage exhibit more pronounced permeability changes compared with the first stage. In the surrounding rock far from the chamber surface, the permeability change is still dominated by damage, while the intermediate transition zone is affected by the coupled effect of capillary pressure and damage.

The third stage is the permeability change dominated by capillary pressure (60–325 d). In this stage, a large amount of CO_2 enters the chamber surrounding rock, and the CO_2 saturation in the surrounding rock reaches the residual saturation. At this point, capillary pressure becomes the dominant factor in permeability evolution. As can be seen in the cloud map, a closed circle of decreased permeability eventually forms along the chamber boundary, as shown in Figure 15. The self-sealing zone is a state in which the permeability of the surrounding rock is substantially reduced after the CO_2 saturation reaches the residual saturation and the permeability is corrected. Once the self-sealing zone is formed, the chamber CO_2 storage system gradually stabilizes, and CO_2 is locked in the chamber by the capillary pressure in the chamber surrounding rock.

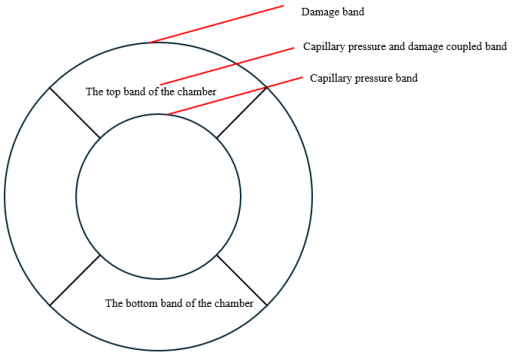


Figure 14. Schematic diagram of permeability variation in the second stage

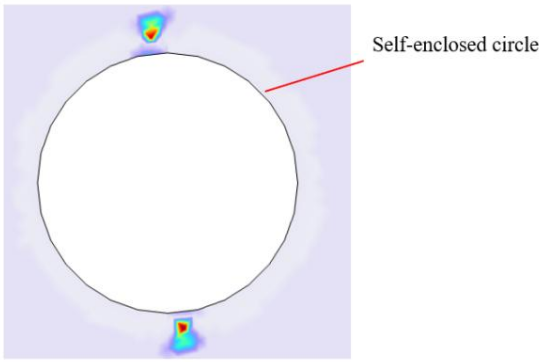


Figure 15. Schematic diagram of permeability variation in the third stage

To quantify the chamber storage efficiency, the remaining CO_2 content in the chamber is calculated. According to the mass conservation equation, the expression is:

$$M_{dt} = M_{d0} - M_{outlet} \tag{23}$$

Where M_{dt} is the remaining CO_2 content in the chamber at time t, and M_{d0} is the initial CO_2 content.

Integrating the CO_2 mass flow rate flowing out of the chamber boundary over time yields the total outflow mass of CO_2 over a period:

$$M_{outlet} = \int_{t1}^{t2} M_v dt \tag{24}$$

Where M_v is the mass flow rate, calculated by Eq. (21).

Finally, the expression for the remaining CO_2 content in the chamber is:

$$M_{dt} = M_{d0} - \int_{t1}^{t2} M_v dt \tag{25}$$

According to Eqs. (21) and (25), the CO_2 content and mass flow rate flowing out of the chamber edge are calculated, as shown in Figure 16. The initial mass flow rate is 2.36×10^{-5} g/d, with a maximum of 3.18×10^{-5} g/d. The increase in mass flow rate in the early stage is due to damage in the chamber surrounding rock, which increases the permeability of the surrounding rock. The CO_2 mass flow rate gradually decreases over time because the CO_2 saturation around the chamber surrounding rock reaches a threshold and forms a self-sealing zone. In the model, when the CO_2 saturation exceeds the residual saturation, the permeability is corrected by the saturation correction coefficient ks. The mass flow rate at the final moment is 1.05×10^{-5} g/d. The mass flowing out of the chamber edge gradually increases over time, totaling 452.63 kg at 365 days.

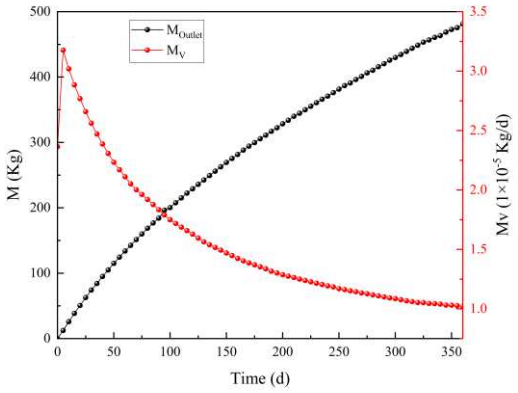


Figure 16. Variation curves of CO_2 mass flow rate and CO_2 seepage content at the chamber boundary over time.

According to the ideal gas equation, the initial CO_2 storage amount in the chamber is calculated to be 35.4 t CO_2. According to Eq. (23),Theremaining CO_2 content in the chamber is calculated, as shown in Figure 17. Initially, 35.4 t CO_2 was stored in the chamber, and it gradually decreased over time. In the early stage, due to damage and the initial pressure difference, the CO_2 seepage rate was relatively fast. As time progressed, the pressure difference between the chamber interior and the surrounding rock decreased, and the CO_2 in the surrounding rock approached the residual saturation. Under the coupling of capillary pressure and reduced pressure difference, the CO_2 seepage rate slowed down, and finally 34.95 t Cof CO_2remained in the chamber.

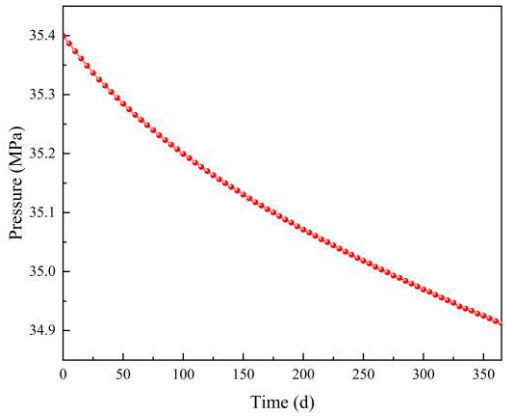


Figure 17. CO_2 storage content–time curve in the chamber

The CO_2 leakage rate during storage is defined as Mleak, expressed as:

$$M_{leak} = \frac{M_{outlet}}{M_{d0}} \times 100\% \tag{26}$$

According to Eq. (26), the variation curve of M_{leak} over time is obtained, as shown in Figure 18. The CO_2 leakage rate gradually increases over time, reaching a maximum of 1.28%, which means the storage efficiency of the chamber within one year reaches 98.72%.

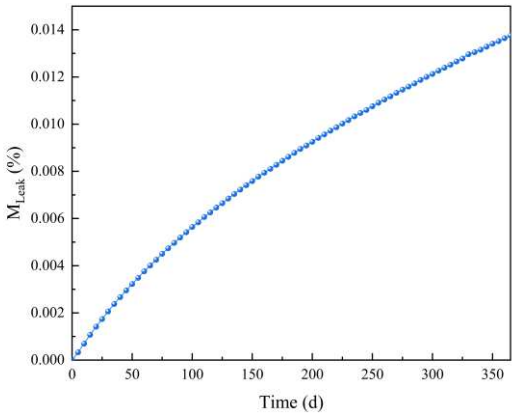
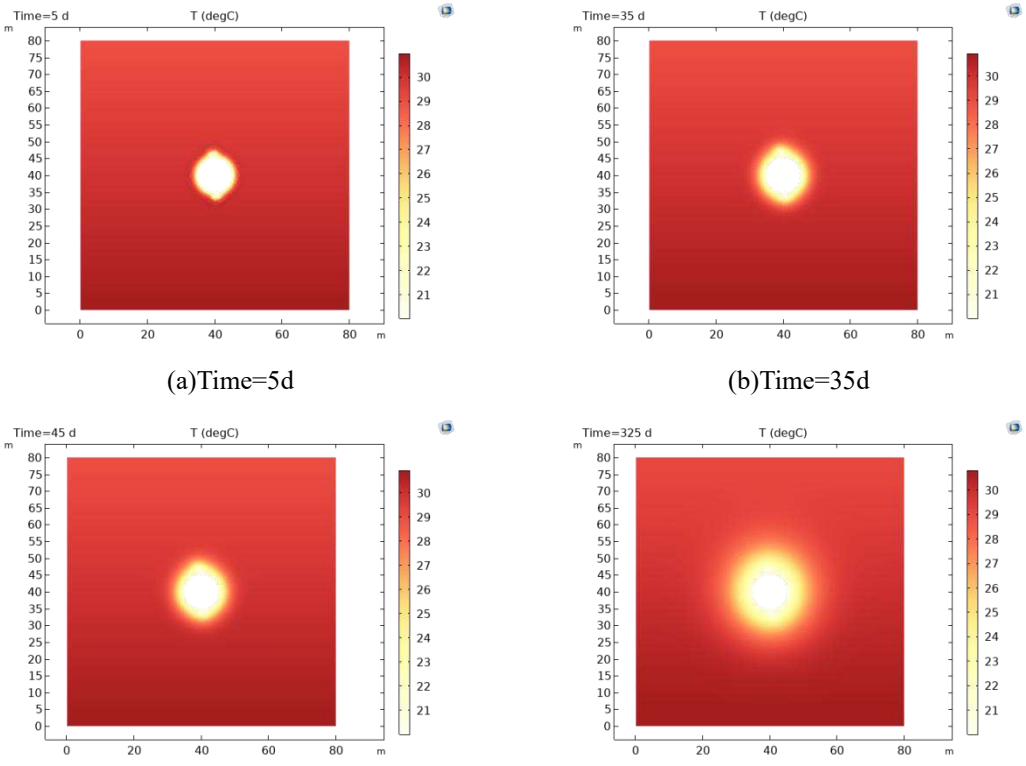


Figure 18. CO_2 leakage rate–time curve

4.3 Temperature Field Analysis

Figure 19 presents the temperature cloud maps during the CO_2 seepage process along the chamber surrounding rock. Figure 19(a)–(d) show the temperature variation cloud maps of the chamber surrounding rock at 5, 35, 45, and 325 days, respectively. It can be seen that the temperature gradually decreases as CO_2 seeps along the chamber. This is because the CO_2 inside the chamber is in a high-pressure gaseous state. When CO_2 seeps outward through the micro-cracks and pores of the surrounding rock, it flows from a high-pressure region (the chamber) to a low-pressure region (the deeper surrounding rock or farther away). This process is an adiabatic expansion, during which the CO_2 temperature decreases. Low-temperature CO_2 and normal-temperature surrounding rock appear along the seepage path, and a temperature difference exists.sts between them. Heat is transferred from the surrounding rock to the low-temperature CO_2, cooling the surrounding rock. In the early stage of storage, the temperature decreases rapidly in the vertical direction of the chamber but changes slowly in the horizontal direction. The rate of temperature change is influenced by CO_2

flow. According to the analysis of the fluid mass transfer field, CO_2 mainly seeps through the roof of the chamber surrounding rock in the early stage. As time progresses, the temperature decrease rate of the chamber surrounding rock tends to stabilize, showing a trend of heat dissipation from the chamber center outward in all directions. This is consistent with the analysis of the fluid mass transfer field. Since the essence of heat transfer is heat exchange between CO_2 and the surrounding rock, in the later stage of storage, CO_2 accumulates near the chamber surrounding rock due to capillary pressure and forms a closed circle around the surrounding rock, resulting in a consistent temperature decrease trend in all directions.

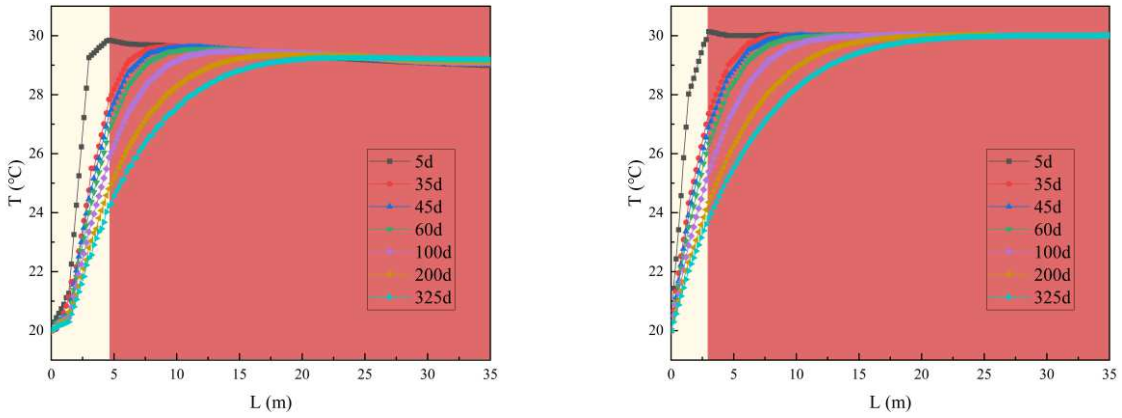


(a)Time=5d (b)Time=35d

(c)Time=45d (d)Time=325d

Figure 19. Temperature cloud maps of the chamber surrounding rock

According to the cloud maps, the temperature distributions at the left and right sidewalls and at the roof and floor are nearly symmetrical. Therefore, the temperature at the roof and left sidewall monitoring lines of the chamber was selected to study the temperature variation of the chamber surrounding rock. Figure 20 shows the temperature variation curves of the monitoring lines at the roof and left sidewall of the chamber surrounding rock over time. The horizontal axis L represents the distance from the chamber wall. As shown in Figure 20, the closer to the chamber wall, the faster the temperature decreases. Taking 5 d in Figure 20(a) as an example, the location with the greatest temperature influence is defined as the cooling zone, i.e.The yellow part in the figure is the cooling zone, while the red part is the unaffected zone with relatively small temperature influence. At 5 d, the cooling zone extends 4.52 m from the roof wall of the chamber. As time progresses, the cooling zone gradually expands. Comparing the cooling zones at the roof and left sidewall of the chamber, in the initial stage, the cooling zones at these two locations are 4.52 m and 2.92 m, respectively, indicating that CO_2 mainly undergoes heat exchange along the roof and floor of the chamber in the early stage. As time progresses, the difference in the cooling zone gradually decreases. At 325 d, the cooling zones at both the left sidewall and the roof reach 22.16 m.



(a) Temperature variation curve at the roof monitoring line of the chamber

(b) Temperature variation curve at the left sidewall monitoring line of the chamber

Figure 20. Temperature variation curves of the monitoring lines

4.4 Analysis of CO_2 in the Chamber under Different Cases

To systematically evaluate the storage performance of deep underground chambers, this study conducted quantitative simulations of CO_2 storage processes at three depths: 500 m, 800 m, and 1200 m, with actual storage amount and storage efficiency as the core evaluation indicators. Figure 21 shows that under the three cases, the CO_2 escape rate in the chamber exhibits a "fast first, then slow" characteristic. In the early stage of storage, damage to the surrounding rock induced by high-pressure injection leads to a temporary increase in permeability. Subsequently, CO_2 fills the natural pores and triggers the capillary trapping effect, forming a self-sealing zone that significantly slows down the escape. In terms of specific data, the initial injection amounts for Cases 1, 2, and 3 are 35.4 t, 50.55 t, and 68.55 t, respectively, and the actual retained amounts after one year are 34.91 t, 50.27 t, and 67.99 t, respectively. The storage amount increases significantly with depth, mainly because the deep high-pressure and suitable temperature environment allows CO_2 to maintain a high-density supercritical state, greatly enhancing the physical storage capacity per unit volume.

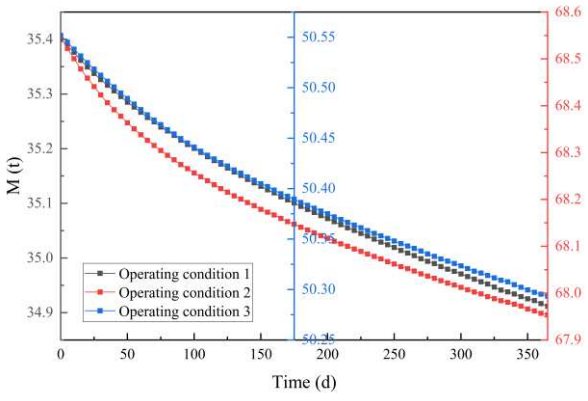


Figure 21. CO_2 storage amount–time curve in the chamber under different cases

In terms of long-term safety assessment, Figure 22 shows the evolution of CO_2 storage efficiency in the chamber. Affected by continuous seepage through the pores and fractures of the surrounding rock, the storage efficiency under the three cases gradually decreases over time. However, at the end of the one-year storage period, the final storage efficiencies of Cases 1, 2, and 3 remain stable at 98.72%, 99.48%, and 99.24%,

respectively, indicating that the deep underground chamber possesses extremely high storage reliability overall. It is worth noting that the final storage efficiency does not increase linearly with depth but exhibits a nonlinear characteristic of first increasing and then decreasing. This phenomenon is controlled by the multi-field coupling mechanism of phase transition and mechanical response: at 500 m (gaseous state), the dynamic viscosity of CO_2 increases with increasing temperature; when the depth increases to 800 m, CO_2 transitions to a supercritical state, and the overall storage efficiency reaches its optimum; however, when the depth further extends to 1200 m, the dynamic viscosity of supercritical CO_2 decreases due to the continued increase in temperature, and its fluidity increases. Combined with the damage-induced dilatancy effect of the surrounding rock induced by deep high in-situ stress, the leakage amount eventually increases and the storage efficiency decreases. This pattern indicates that in actual engineering site selection, there exists an "optimal depth window" that balances storage capacity and storage safety.

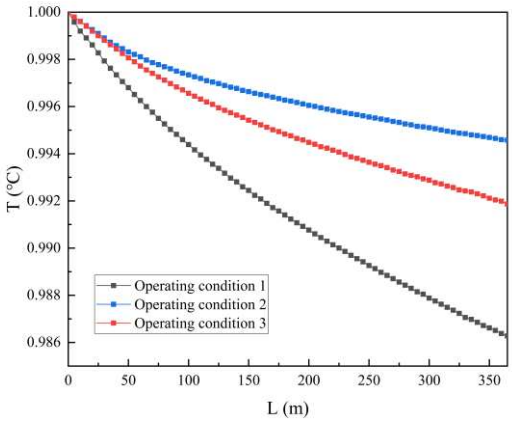


Figure 22. Storage efficiency–time curve of the chamber under different cases

5. Conclusions

This study established a coupled thermo–hydro–mechanical (THM) numerical simulation model based on the coupling of capillary pressure and surrounding rock damage, and conducted numerical simulation experiments on CO_2 storage in underground chambers. The seepage laws of CO_2 along the chamber surrounding rock during chamber storage, as well as the temperature distribution of the chamber surrounding rock during the seepage process, were clarified. Based on the variation of CO_2 storage efficiency in underground chambers under three cases, theoretical support is provided for the evaluation of CO_2 storage efficiency in underground chambers. The main conclusions are as follows:

(1)Surrounding rock damage and CO_2 seepage exhibit a significant directional synergistic effect. Chamber surrounding rock damage preferentially propagates along the direction of higher initial in-situ stress, causing CO_2 to easily form a preferential seepage pathway along this direction. Therefore, in actual engineering, monitoring networks should be deployed at the far end of the maximum principal stress direction to prevent concealed gas leakage.

(2)The seepage and migration of CO_2 are accompanied by significant heat exchange, resulting in a localized temperature decrease in the surrounding rock mass. This specific thermal physical response can serve as an early key warning indicator for monitoring whether CO_2 leakage occurs in actual engineering.

(3)Storage depth has a nonlinear influence on CO_2 storage efficiency. Constrained by the combined effects of CO_2 phase transition and deep high-stress-induced damage, the storage efficiency shows a trend of first increasing and then decreasing with increasing depth. In this simulation, when the depth increased from 500 m to 800 m, the storage efficiency increased by 0.76%; however, when the depth increased to 1200 m, the efficiency

decreased by 0.24% instead. This indicates that there exists an "optimal depth window" for deep chamber storage that balances safety and efficiency.

Author Contribution

Z.T. was responsible for the overall conceptualization of the study, developed the methodology, and provided resources, supervision, project administration, and funding acquisition. Y.Z. conducted the formal analysis, performed the validation and investigation, and wrote the original draft of the paper. Y.L. and Z.X. carried out the software simulation. L.M., S.L., and Y.Z. performed the validation. L.M. and Y.Z. conducted the investigation. Y.L. and S.L. were responsible for data curation. L.M. and Z.X. offered suggestions to improve the manuscript during review and editing. Y.L. and Y.Z. created the visualization. All authors have read and agreed to the published version of the manuscript.

Funding

This work was supported by the National Natural Science Foundation of China (Grant No. 52464019), the Natural Science Foundation of Inner Mongolia (Grant No. 2024LHMS05031), and the Inner Mongolia Key R&D and Achievement Transformation Plan Project (Grant No. 2025SYFHH0687).

Data Availability Statement

The data that support the findings of this study are available from the corresponding author upon reasonable request. The numerical simulation data are presented in the manuscript in the form of tables and figures.

Competing Interests

The authors have no relevant financial or non-financial interests to disclose.

References

[1] Li XC, Fang ZM, Wei N, Bai B (2009) Discussion on the technical roadmap of CO_2 capture and storage in China. Rock Soil Mech 30 (9):2674–2678, 2696. https://doi.org/10.16285/j.rsm.2009.09.005 (in Chinese)

[2] Wei HF, Fang J, Shi JJ et al (2025) Theory, technology, and prospects of deep underground storage space utilization. Coal Geol Explor 53(2):67–83 (in Chinese)

[3] Cui ZD, Liu DA, Zeng RS (2010) CO_2 geological storage and sustainable development in China. China Popul Resour Environ 20(3):9–13 (in Chinese)

[4] Li SH, Zheng MC, Lu T et al (2025) Geological characteristics of carbon dioxide storage in deep saline aquifers of sedimentary sags. China Well Rock Salt 56(3):17–18, 25 (in Chinese)

[5] Szulczewski ML, MacMinn CW, Herzog HJ, Juanes R (2012) Lifetime of carbon capture and storage as a climate-change mitigation tec hnology. Proc Natl Acad Sci USA 109(14):5185–5189. https://doi.org/10.1073/pnas.1115347109

[6] Yang SG, Li XC, Cai MY et al (2023) Overseas management systems and standards for CO_2 geological storage and their implications f or China. Nat Gas Ind 43(12):130–137 (in Chinese)

[7] Wang GF, Li Y, Wang R et al (2024) New progress in CO_2 geological storage and utilization. Oil Gas Geol 45(4):1168–1179 (in Chines e)

[8] Gao H, Luo K, Li T et al (2025) Impact of CO_2 injection on mineral composition, pore structure, and mechanical properties of tight sa ndstone reservoirs: implications for CO_2 geosequestration. Geoenergy Sci Eng 254:214067

[9] Yang M, Yang Z, Wu M, Sun H, Yu T, Chen B, Song Y (2025) Study on characteristics of CO_2 seepage within natural gas hydrate res ervoirs. Int J Heat Mass Transfer 252:127452. https://doi.org/10.1016/j.ijheatmasstransfer.2025.127452

[10] Zhang T, Li JX, Zhu Y, Rudolph V, Chen Z (2025) Impact of gas adsorption on coal relative permeability: a laboratory study. Int J Roc k Mech Min Sci 194:106191. https://doi.org/10.1016/j.ijrmms.2025.106191

[11] Yin SG, Yang GD, Feng T et al (2023) Effects of shale reservoir physical parameters on different CO_2 storage mechanisms and storage capacity. Geol J China Univ 29(1):37–46. https://doi.org/10.16108/j.issn1006-7493.2022071 (in Chinese)

[12] Guo P, Li XH, Sun Z et al (2019) Numerical simulation of CO_2 flooding and storage in low-permeability gas reservoirs. Sci Technol Eng 19(23):68–76 (in Chinese)

[13] Li A, Shi TL, Su CY et al (2025) Study on CO_2 enhanced coalbed methane extraction effect based on different reservoir parameters and injection timing. Coal Mine Saf 56(8):1–13. https://doi.org/10.13347/j.cnki.mkaq.20241605 (in Chinese)

[14] Peng WR, Xing L, Li QQ et al (2025) Seismic monitoring method for CO_2 seabed saline aquifer storage sweep range: a case study of the Sleipner CCS project. Mar Geol Quat Geol 45(1):210–224. https://doi.org/10.16562/j.cnki.0256-1492.2024040401 (in Chinese)

[15] Mahgoub SA, Abedi S (2026) Micro-scale examination of altered fracture properties in shale rocks exposed to CO_2-rich brine under high-temperature and high-pressure conditions. Rock Mech Rock Eng 59(1):65–86. https://doi.org/10.1007/s00603-025-04870-5

[16] Zhou Y, Tang L, Song Z, Pan B, Yue M, Liu J, Song H (2024) Research on CO_2 sequestration in saline aquifers with different relative permeability considering CO_2 phase conditions. Energy 313:133739. https://doi.org/10.1016/j.energy.2024.133739

[17] Yu H, Yang J, Li W, Luo W, Kang H (2024) Study on fluid phase behavior characteristics of low permeability reservoir under different CO_2 injection amounts. Energy Rep 12:2297–2305. https://doi.org/10.1016/j.egyr.2024.08.024

[18] Pan J, He H, Li G, Wang X, Hou Q, Liu L, Cheng N (2023) Anisotropic strain of anthracite induced by different phase CO_2 injection and its effect on permeability. Energy 284:128619. https://doi.org/10.1016/j.energy.2023.128619

[19] Dan WD, Li X, Wang FG (2025) Experimental study on breakthrough pressure of caprock for carbon storage in saline aquifers under different CO_2 phase states. Coal Geol Explor 53(10):141–150 (in Chinese)

[20] Lei G, Ren JF, Liu BK et al (2025) Physical property evolution of Longmaxi shale under supercritical CO_2–water–rock interaction and its influence on wellbore stability. Nat Gas Ind 45(5):136–149 (in Chinese)

[21] Cui GD, Hu Z, Ning FL et al (2023) Capillary force trapping mechanism in saline aquifers and its influence on impure CO_2 storage efficiency. J China Coal Soc 48(7):2791–2801. https://doi.org/10.13225/j.cnki.jccs.CN23.0222 (in Chinese)

[22] Yao YB, Sun XX, Wan L (2023) Microscopic mechanism of CO_2 geological storage in coal seams. Coal Geol Explor 51(2):146–157 (in Chinese)

[23] Guo CB, Wang ZH, Liu K et al (2019) Application and research status of special underground space. Geol China 46(3):482–492 (in Chinese)

[24] Wang X, Yang PF, Liang B et al (2025) Study on thermal-hydraulic-mechanical coupling effect of CO_2 storage in deep saline aquifers based on an improved homogenization model. J China Univ Min Technol 54(2):399–412. https://doi.org/10.13247/j.cnki.jcumt.20240453 (in Chinese)

[25] Wang YY, Peng XY, Wang XG et al (2023) CO_2 migration mechanism in layered saline aquifers under the synergistic effect of buoyancy and capillary force. J China Univ Pet (Nat Sci Ed) 47(3):96–106 (in Chinese)

[26] Hu P (2021) Application of multi-field coupling model in CO_2 saline aquifer storage analysis. PhD thesis, Dalian Univ of Technology. https://doi.org/10.26991/d.cnki.gdllu.2021.001982 (in Chinese)

[27] Zhang B, Liang KQ, Wang WB et al (2019) Evaluation of effective CO_2 geological storage potential in deep saline aquifers of the Ordos Basin. Unconv Oil Gas 6(3):15–20 (in Chinese)

[28] Liu B, Shi CS (2025) Injection well site optimization of carbon geological sequestration based on dynamic programming. Chin J Eng 47(6):1377–1386. https://doi.org/10.13374/j.issn2095-9389.2024.03.18.001 (in Chinese)

[29] Zhou YB, Wang R, He YF et al (2023) Typical case analysis and comparison of CO_2 geological storage in saline aquifers. Pet Geol Recovery Effic 30(2):162–167. https://doi.org/10.13673/j.cnki.cn37-1359/te.202201028 (in Chinese)

[30] Song TT, Wang XH, Ni FP et al (2025) Application research on CO_2 geological utilization and storage monitoring based on the eddy covariance method. Environ Monit China 41(5):229–237. https://doi.org/10.19316/j.issn.1002-6002.2025.05.23 (in Chinese)